nature materials

LETTERS

https://doi.org/10.1038/s41563-019-0463-8

Ultrahigh-current-density niobium disulfide catalysts for hydrogen evolution

Jieun Yang[1,10], Abdul Rahman Mohmad[2,10], Yan Wang[1], Raymond Fullon[1], Xiuju Song[1,3], Fang Zhao[4], Ibrahim Bozkurt[1], Mathias Augustin[5], Elton J. G. Santos[5*], Hyeon Suk Shin[6], Wenjing Zhang[3], Damien Voiry[7], Hu Young Jeong[8*] and Manish Chhowalla[1,3,9*]

Metallic transition metal dichalcogenides (TMDs)[1–8] are good catalysts for the hydrogen evolution reaction (HER). The overpotential and Tafel slope values of metallic phases and edges[9] of two-dimensional (2D) TMDs approach those of Pt. However, the overall current density of 2D TMD catalysts remains orders of magnitude lower (~10–100 mA cm^{-2}) than industrial Pt and Ir electrolysers (>1,000 mA cm^{-2})[10,11]. Here, we report the synthesis of the metallic 2H phase of niobium disulfide with additional niobium (2H $Nb_{1+x}S_2$, where x is ~0.35)[12] as a HER catalyst with current densities of >5,000 mA cm^{-2} at ~420 mV versus a reversible hydrogen electrode. We find the exchange current density at 0 V for 2H $Nb_{1.35}S_2$ to be ~0.8 mA cm^{-2}, corresponding to a turnover frequency of ~0.2 s^{-1}. We demonstrate an electrolyser based on a 2H $Nb_{1+x}S_2$ cathode that can generate current densities of 1,000 mA cm^{-2}. Our theoretical results reveal that 2H $Nb_{1+x}S_2$ with Nb-terminated surface has free energy for hydrogen adsorption that is close to thermoneutral, facilitating HER. Therefore, 2H $Nb_{1+x}S_2$ could be a viable catalyst for practical electrolysers.

Ultrathin layers of transition metal dichalcogenide (TMD) catalysts exhibit improved electrocatalytic performance due to efficient charge injection and transfer to active sites[13,14]. Increasing the conductivity via engineering of metallic phases[2,15,16] and edges[14,17–19] also leads to substantial improvement in catalytic properties. To this end, the metallic 1T phase of semiconducting MoS_2 induced by lithium chemistry[1,2,20] has been widely studied for hydrogen evolution reaction (HER) catalysis. Recently, multilayers of thin metallic TMDs such as NbS_2 (ref. [4]), TaS_2 (ref. [5]) and VS_2 (ref. [7]) have also been studied for HER. The key advantage of metallic TMDs according to theory is that the basal plane is catalytically active for the HER[4,21,22], unlike in semiconducting MoS_2 where only the metallic edges are active[9]. However, in contrast with noble metal catalysts such as Pt nanoparticles, the electronic structure of atomically thin materials is strongly influenced by local electrochemical reactions. For example, in the case of metallic 1T phase MoS_2, the adsorption of protons on the surface—the first step in the HER—can dramatically reduce the conductivity of the two-dimensional (2D) nanosheets[21], which can slow down the reaction kinetics and reduce the overall current density. Thus, a fine balance must be achieved between reducing the thickness of catalysts and maintaining metallic nature of 2D materials to maximize catalytic performance.

NbS_2 is a layered material that can exist in the hexagonal (2H phase) or rhombohedral (3R) crystal configurations (see Supplementary Fig. 1a,b,d,e). Metallic 2H phase NbS_2 has been predicted to be one of the most efficient electrocatalysts for the HER among the different types of TMDs[22]. In addition to the 2H and 3R phases, an unexplored non-layered (three-dimensional, 3D) polytype with $Nb_{1+x}S_2$ (where x is ~0.35) stoichiometry, first synthesized in 1960 (ref. [12]), consisting of excess niobium between NbS_2 layers is also stable (see Supplementary Fig. 1c,f). We find that the $Nb_{1+x}S_2$ phase can be synthesized by adjusting the chemical vapour deposition (CVD) growth parameters (see Methods). An atomic force microscopy image of typical $Nb_{1+x}S_2$ crystals synthesized by CVD is shown in Fig. 1a. Films of varying thicknesses ranging from 2 nm to 50 nm with lateral dimensions of ~0.5–1 μm were realized by CVD on substrates such as SiO_2 and glassy carbon. We find that the phase of NbS_2 is dependent on the thickness of the material (Supplementary Fig. 2a–c). The electron diffraction patterns corresponding to the phases as a function of thickness are provided in Supplementary Fig. 2d,e. In particular, 2H $Nb_{1+x}S_2$ is predominantly observed in crystals with thickness of less than ~20 nm whereas the 3R phase is primarily stable for thicker samples. High-angle annular dark field (ADF) cross-sectional scanning transmission electron microscopy (STEM) images of $Nb_{1+x}S_2$ clearly reveal excess Nb in both the 2H phase (Fig. 1b) and the 3R phase (Fig. 1c). The spacing $d_{(0002)}$ for the 2H excess Nb phase (6.35 Å, $c = 12.60$ Å) was found to be close to the theoretical value of the $Nb_{1.35}S_2$ composition. The lower contrast in the ADF image of the excess Nb planes is attributed to partial occupation of these sites (an occupancy of 0.35 in the excess layers versus 1 in the NbS_2 2H and 3R layers). Additional evidence for excess Nb atoms in the form of Z contrast scans of atoms and chemical analyses are provided in Supplementary Fig. 3a,b. The X-ray diffraction spectrum shown in Supplementary Fig. 3c provides additional evidence for the non-layered hexagonal phase of $Nb_{1.35}S_2$.

The catalytic properties of NbS_2 and other metallic TMDs such as TaS_2 and VS_2 have been measured in several studies[4,5,7]. The results

[1]Materials Science and Engineering, Rutgers University, Piscataway, NJ, USA. [2]Institute of Microengineering and Nanoelectronics, National University of Malaysia, Bangi, Malaysia. [3]Collaborative Innovation Center for Optoelectronic Science & Technology, International Collaborative Laboratory of 2D Materials for Optoelectronics Science and Technology of Ministry of Education, College of Optoelectronic Engineering, Shenzhen University, Shenzhen, China. [4]Department of Physics, Princeton University, Princeton, NJ, USA. [5]School of Mathematics and Physics, Queen's University, Belfast, UK. [6]Department of Chemistry and Department of Energy Engineering, Low-Dimensional Carbon Materials Center, Ulsan National Institute of Science and Technology, Ulsan, Republic of Korea. [7]Institut Européen des Membranes, University of Montpellier, Montpellier, France. [8]UNIST Central Research Facilities and School of Materials Science and Engineering, Ulsan National Institute of Science and Technology, Ulsan, Republic of Korea. [9]Present address: Department of Materials Science and Metallurgy, University of Cambridge, Cambridge, UK. [10]These authors contributed equally: Jieun Yang, Abdul Rahman Mohmad. *e-mail: e.santos@qub.ac.uk; hulex@unist.ac.kr; mc209@cam.ac.uk

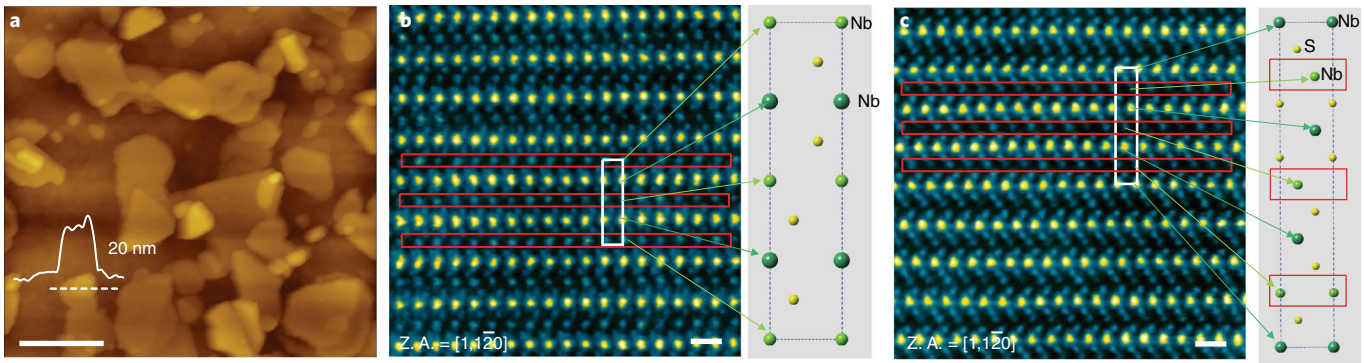

Fig. 1 | Images of $Nb_{1+x}S_2$ crystals and atomic structure. a, Atomic force microscopy image of as-grown $Nb_{1+x}S_2$ ($x \sim 0.35$) crystals on high-quality glassy carbon (scale bar, 1 μm). The roughness profile along the dashed line is shown. **b**, Cross-sectional ADF STEM image of 2H phase $Nb_{1.35}S_2$ and 3R phase $Nb_{1+x}S_2$, **c**. The white rectangles in STEM images in **b** and **c** represent the unit cells of the structures and the corresponding ball and stick models of the unit cell are shown on the right of each STEM image. The red rectangles in the STEM images and the schematic indicate the positions of the excess Nb. Since these sites are partially occupied, the contrast of these planes is lower than of the fully occupied Nb sites. The arrows correlate the locations of the atoms in the STEM images with the atoms in the unit cells. The dark green arrows and spheres in the schematics indicate fully occupied Nb sites and light green arrows and spheres in unit cells indicate partially occupied Nb atoms. Z.A. refers to the zone axis of the crystal structure. Scale bar, 5 Å.

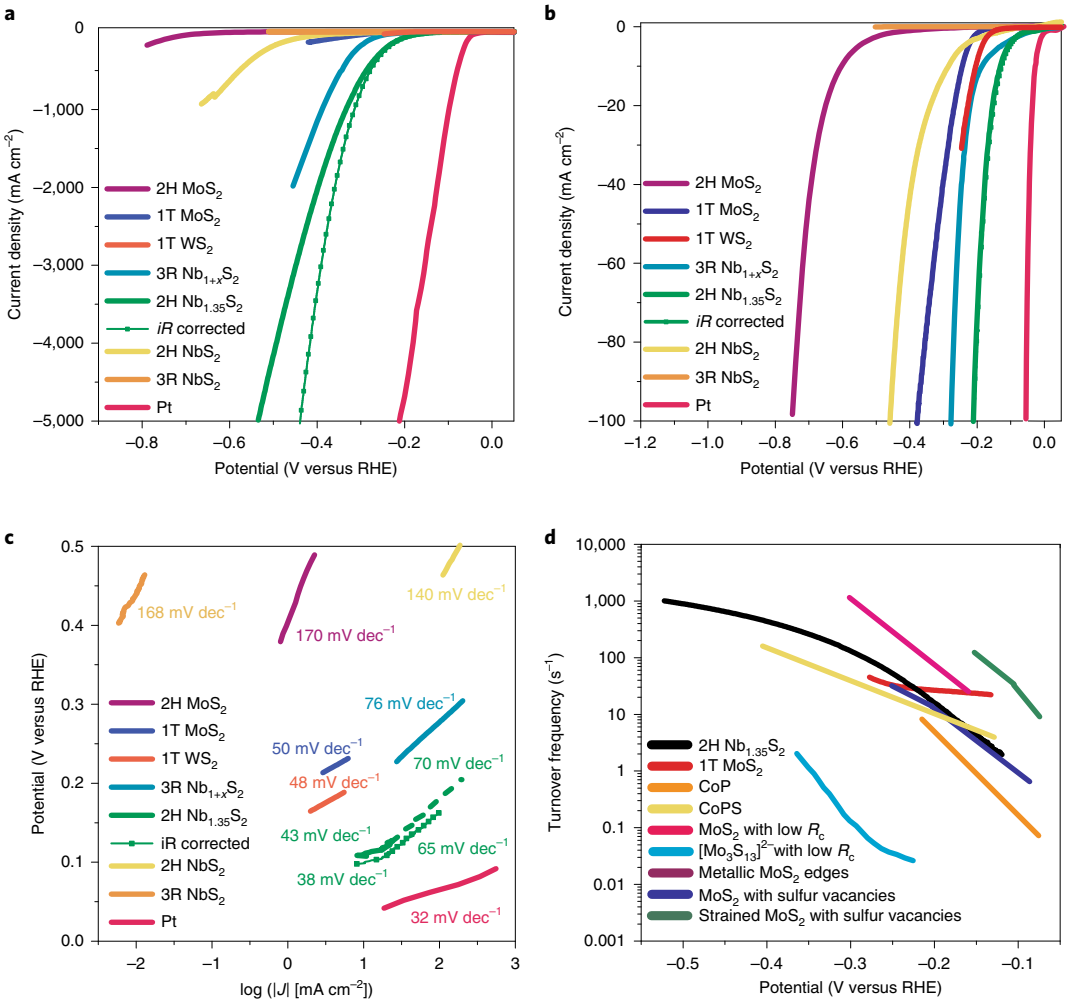

Fig. 2 | HER catalytic activities of different TMDs. a, Polarization curves for 2H MoS_2, 1T MoS_2 and WS_2, 2H $Nb_{1.35}S_2$, 3R $Nb_{1+x}S_2$, 2H NbS_2 and 3R NbS_2 and Pt measured in 0.5 M H_2SO_4 with a scan rate of 5 mV s^{-1}. **b**, Expanded view of the low overpotential region in **a**. The reaction starts immediately on application of voltage, indicating that the onset potential of 2H $Nb_{1.35}S_2$ is <100 mV and the overpotential is 150 mV. **c**, Tafel slopes of different catalysts obtained from the polarization curves in **a**. 2H $Nb_{1.35}S_2$ shows a slope of 43 mV dec^{-1} (38 mV dec^{-1} after *iR* correction) at low overpotentials (100–130 mV, green) and 70 mV dec^{-1} (65 mV dec^{-1} after *iR* correction) at high overpotentials (130–200 mV, red). **d**, TOF values of the 2H $Nb_{1.35}S_2$ (black line), transition metal phosphide and phosphosulfide, and other MoS_2-based catalysts reported in the literature[25–28]. MoS_2 basal planes with sulfur vacancies (blue)[29], strained MoS_2 basal planes with sulfur vacancies (green)[29] and MoS_2 with low charge transfer resistance, R_c (magenta)[15].

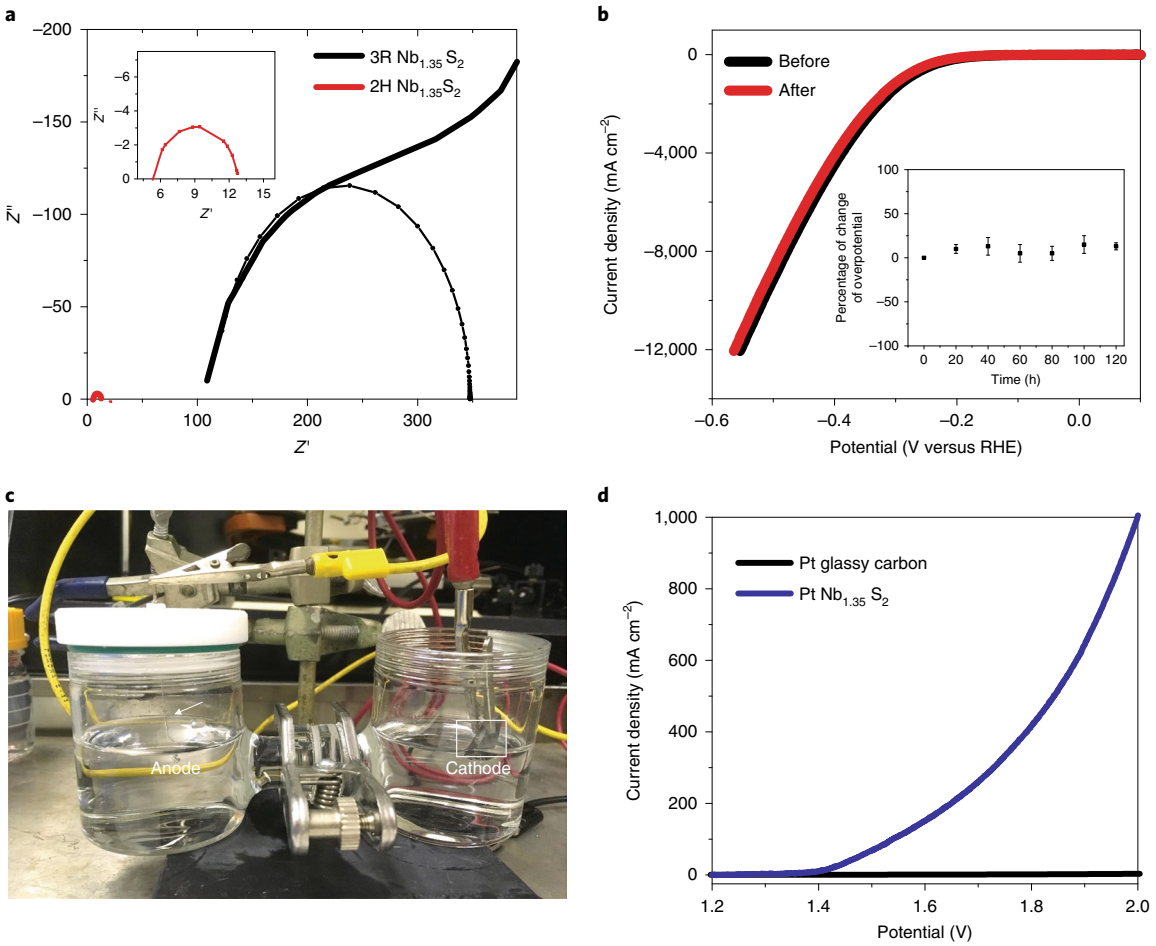

Fig. 3 | Electrochemical impedance spectroscopy, electrochemical stability of $Nb_{1.35}S_2$ and a proof-of-concept electrolyser demonstration. a, Nyquist plots of 2H phase (red curve) and 3R phase $Nb_{1+x}S_2$. Magnification of the 2H $Nb_{1.35}S_2$ plot is shown in the inset. The plots were fitted using an equivalent circuit to extract the series and charge transfer resistances. The axes labels Z' and Z'' are the real and imaginary, respectively, parts of the impedance with units of Ω cm^2. **b**, Polarization curves of 2H $Nb_{1.35}S_2$ before (black curve) and after (red curve) 10,000 cycles. The inset shows the percentage of change in the overpotential. The error bars (s.d.) are obtained from at least five measurements. **c**, Photograph of the two-electrode electrolyser device consisting of a commercial Pt anode and a 2H $Nb_{1.35}S_2$ cathode. **d**, Volt-ampere curves of overall water splitting with 2H $Nb_{1.35}S_2$ as the cathode, while using Pt as the anode. The current density reaches up to 1,000 mA cm^{-2}.

generally reveal Tafel slopes of ~40 mV dec^{-1} and low overpotential values of tens of millivolts versus a reversible hydrogen electrode (RHE). For comparison, the overpotential at which HER proceeds for Pt nanoparticles is 0 V versus a RHE with a corresponding Tafel slope of ~30 mV dec^{-1}. Despite the promising overpotentials and Tafel slopes achieved with metallic TMD catalysts, the maximum reported current density value has remained around ~100 mA cm^{-2}. The current density is limited by the multiple layers of metallic TMDs. That is, in contrast to phase-transformed 1T metallic MoS_2 nanosheets that are single layered, it is generally challenging to synthesize or exfoliate metal TMDs down to the monolayer. Thus, most metallic NbS_2 and TaS_2 catalysts are multilayered and therefore electrons injected from the glassy carbon support must overcome the van der Waals gaps between the layers to reach the active sites on the surface. This increases the charge transfer resistance and thus the catalytic activity has been demonstrated to be inversely related to the number of layers in TMDs[23]. In the case of single layers, while the charge transfer kinetics are improved, the current-carrying capability is lower and therefore the overall current density that can be achieved is also lower. Furthermore, the recombination of protons with free electrons on the surface of the single-layer catalysts (the first step of the reaction) decreases the concentration of free carriers and therefore the conductivity[21], reducing the kinetics of the HER and lowering the current density.

We have tested the catalytic performance of metallic 2H $Nb_{1.35}S_2$ with improved conductivity via elimination of van der Waals gaps between layers. This $Nb_{1.35}S_2$ phase for HER was directly grown at 1,273 K (the CVD parameters are described in Methods) on high-quality glassy carbon electrodes. The HER was measured in 0.5 M H_2SO_4 electrolyte (see Methods for a detailed description of the measurements). The current density as a function of potential (versus a RHE) from 2H and 3R NbS_2 and excess Nb 2H phase $Nb_{1.35}S_2$, along with those from 3R $Nb_{1+x}S_2$, the 2H MoS_2 and 1T phases of MoS_2 and WS_2 (ref. [3]), 2H and 3R NbS_2, and Pt for comparison, are shown in Fig. 2a. It can be clearly seen from the polarization curves that the current density for the 2H $Nb_{1.35}S_2$ is exceptionally large, reaching 1,000 mA cm^{-2} at ~370 mV and 5,000 mA cm^{-2} at ~420 mV, as indicated by the *iR* corrected curve in Fig. 2a. This current density is obtained from careful analyses of the catalytic active area. We have examined numerous scanning electron microscope images to determine the areal coverage of catalyst material on the glassy carbon surface. We found that 20% ± 5% of the electrode surface is covered by the catalyst particles, see Supplementary Fig. 4. In addition to the areal coverage, we also carefully measured the

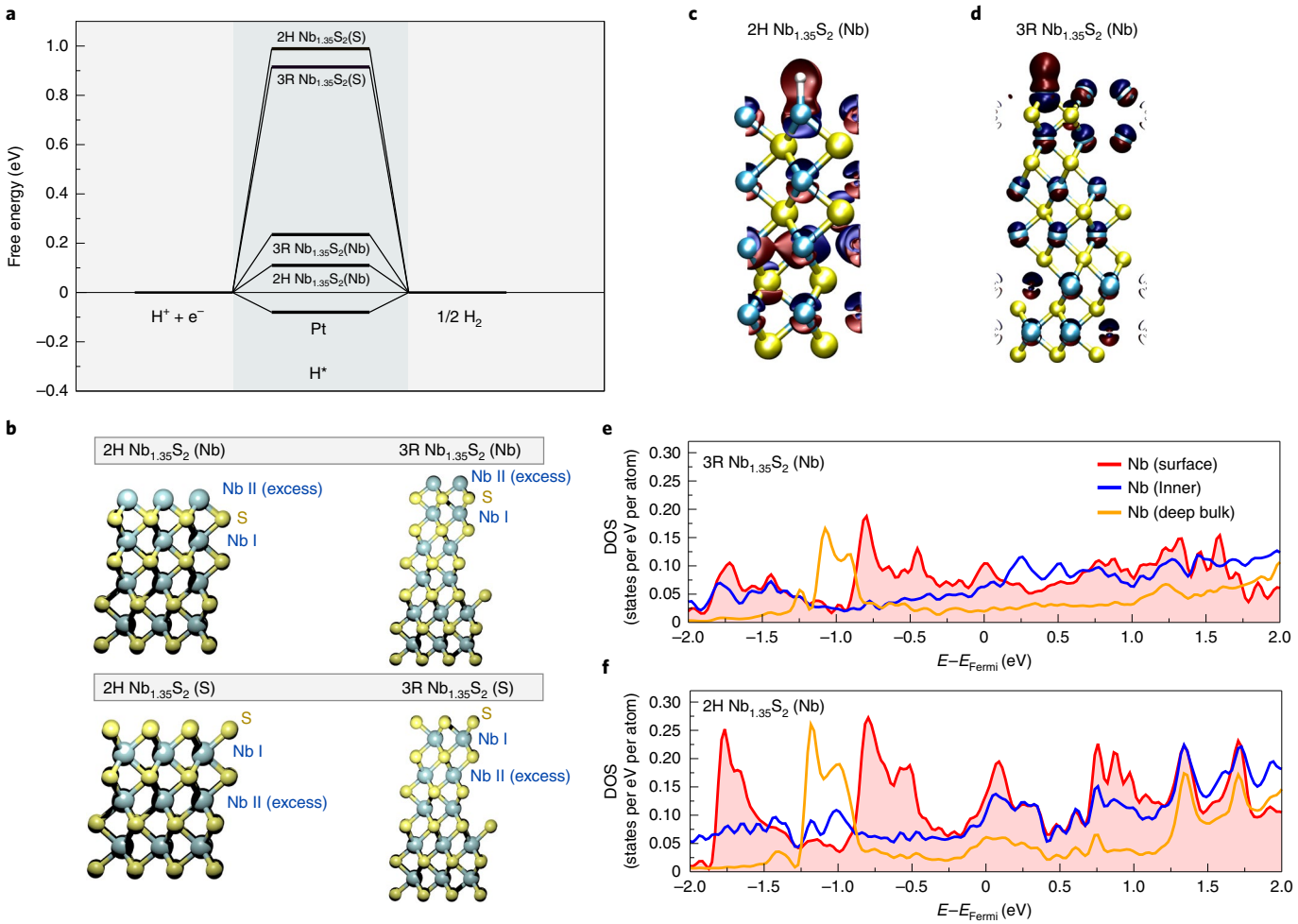

Fig. 4 | Thermodynamic stability and free-energy calculations for hydrogen evolution for the 2H $Nb_{1.35}S_2$ and 3R $Nb_{1.35}S_2$ phases. a, The free-energy diagram for hydrogen evolution at standard conditions (1 bar of H_2 and pH = 0 at 300 K). The energies of the intermediate states are calculated using the BEEF-vdW functional as described in the Methods. A coverage of 0.25 monolayers was used for all calculations. **b**, Optimized geometries for S- and Nb-terminated surfaces of the 2H $Nb_{1.35}S_2$ and 3R $Nb_{1.35}S_2$ phases. **c**,**d**, Charge density difference for H adsorbed on top of Nb-terminated 2H (**c**) and 3R $Nb_{1.35}S_2$ (**d**) phases. Most of the charge is localized on the surface, with clear differences between the 2H and 3R $Nb_{1.35}S_2$ phases (**c** and **d**) with the former having larger magnitudes. **e**,**f**, Density of states (DOS) per atom for the Nb-terminated 2H and 3R $Nb_{1.35}S_2$ phases projected on different Nb sites. Surface Nb, inner Nb and deep bulk Nb atoms are shown in red, blue and orange, respectively. For a better contrast between the different Nb's atoms, the DOS of surface Nb atoms is highlighted with with red shading. The Fermi level is set to 0 eV.

electrochemical surface area (see Supplementary Fig. 5) to find the roughness factor (RF = 11 ± 3). Using this value, we were able to accurately determine the active area of the catalyst and use it to calculate the current density. To complement the current density measurements, we measured the actual amount of evolved hydrogen using a gas chromatograph (GC, Agilent 7890 B) equipped with molecular sieve 5 Å capillary column and a thermal conductivity detector. The measurements were performed in a gas-tight three-electrode cell. Ar gas was purged in the cell to remove air. The thermal conductivity detector cell was calibrated using known hydrogen amounts (5% and 10% H_2 balance Ar certified standard gas). The volume of hydrogen evolved by the 2H $Nb_{1.35}S_2$ electrodes was measured at two overpotentials. We found that 2H $Nb_{1.35}S_2$ can evolve H_2 up to 150 μmol h^{-1} and 300 μmol h^{-1} at 300 mV and 400 mV, respectively. When normalizing the performance to the surface area, the rate of H_2 evolution reaches ~30 l cm^{-2} h^{-1} equivalent to 6 mmol h^{-1} cm^{-2} at 400 mV. The Faradaic efficiency for the HER is typically 100% and therefore the current density is a direct indication of the amount of hydrogen evolved. Thus, careful measurement of the electrochemical surface area to obtain current density is a good indicator of catalyst performance. To confirm this, we measured the Faradaic efficiency (FE) using FE = $\frac{2nF}{Q}$, where n is the amount of hydrogen in moles measured by the GC, F is the Faraday constant, Q is the charge obtained from the measurements in Fig. 2a ($Q = I \times t$, where I is the current and t is the time). The obtained efficiencies are 96% and 100% at 300 mV and 400 mV, respectively. Thus, the GC measurements confirm the electrochemical measurements and provide additional evidence for the high performance of 2H $Nb_{1.35}S_2$.

It can be seen from Fig. 2b, which provides an expanded view of the low overpotential region in Fig. 2a, that the cathodic potential at which the HER starts is less than 100 mV (overpotential of <150 mV) for the 2H $Nb_{1.35}S_2$ catalysts. The reaction for metallic 2H $Nb_{1.35}S_2$ phase starts immediately on application of the potential and proceeds slowly initially but, as the potential is increased, it proceeds rapidly with very high current densities. The Tafel slopes shown in Fig. 2c provide additional information about the rate limiting step in the catalytic performance. Tafel slope values can vary from 30 mV dec^{-1} for Pt—indicating that HER is limited by the

recombination of adsorbed hydrogens—to >120 mV dec^{-1}, where adsorption of protons limits the catalytic activity. It can be seen that the Tafel slope for 2H phase $Nb_{1.35}S_2$ catalysts is 43 mV dec^{-1} (and ~38 mV dec^{-1} after correcting for the internal resistance of the measurements system, *iR* correction) at low overpotentials (100–120 mV), which is comparable to what has been measured for metallic 1T phase MoS_2 and NbS_2 and suggests that the rate limiting reaction is the desorption of hydrogens. At higher potentials (120–250 mV), the Tafel slope increases to ~70 mV dec^{-1} (or 65 mV dec^{-1} after *iR* correction), suggesting that hydrogen adsorption or diffusion of protons to active sites limits the reaction. To differentiate between these two mechanisms, we made HER measurements under agitation to increase diffusion of protons and found that the results are largely unchanged. These observations are consistent with theoretical results that show that, unlike Pt, metallic TMD catalysts such as NbS_2 possess dilute adsorption of hydrogens on the surface at low potentials but the high activity per site is retained at higher potentials, where coverage of adsorbed hydrogens increases[4]. In addition to the overpotential and Tafel slope, we have also measured the number of hydrogen molecules evolved per second (the turnover frequency, TOF) for the catalysts. We have found the TOF for the 2H phase $Nb_{1.35}S_2$ catalysts to be in excess of 100 s^{-1} at 280 mV. The TOF from this work compares favourably with other reports, as summarized in Fig. 2d. The exchange current density at 0 V for the $Nb_{1.35}S_2$ phase catalysts was found to be ~0.8 mA cm^{-2}, which corresponds to a TOF of 0.17 s^{-1}. For comparison, the exchange current density for Pt (111) is 0.5–1 mA cm^{-2}, corresponding to a TOF of ~1 s^{-1} (ref. [9]), and for metallic 2D TMDs the values are 0.02 mA cm^{-2} and 0.043 s^{-1} (ref. [3]), suggesting that the turnover for hydrogen evolution is high for 2H phase $Nb_{1.35}S_2$ catalysts. A summary of the obtained values is provided in Supplementary Table 1.

Impedance measurements on 2H $Nb_{1.35}S_2$ and 3R $Nb_{1+x}S_2$ are shown in Fig. 3a. It can be seen that the series resistance for the 2H phase $Nb_{1.35}S_2$ obtained at 1 MHz, where the phase angle is close to zero, is 3.5 Ω due to its high electrical conductivity and this indicates good contact with the glassy carbon electrode. The charge transfer resistance is 7.4 Ω, which facilitates charge injection and transport to active sites. In contrast, the 3R $Nb_{1+x}S_2$ shows higher resistances and diffusion limited activity. This is in agreement with our observations that the 3R phase is less conducting and is stable at higher film thicknesses. Finally, we have measured the electrochemical stability of the electrodes by carrying out over 10000 cycles. The high current density shows remarkable stability with negligible difference in polarization curves and overpotential values after 10,000 cycles (Fig. 3b). The above experimental results suggest that excess Nb in non-layered $Nb_{1.35}S_2$ allows realization of practical current densities of >5,000 mA cm^{-2}—making them potentially useful alternatives to Pt and Ir. To translate the high current densities of 2H phase $Nb_{1.35}S_2$ catalysts into practical device, we fabricated a proof of concept two electrode electrolyser for water splitting. The device shown in Fig. 3c consists of 2H $Nb_{1.35}S_2$ on glassy carbon cathode and a commercial Pt anode. The measurements were carried out at room temperature in 0.5 M H_2SO_4. The device characteristics are plotted in Fig. 3d, which show that the reaction for the 2H $Nb_{1.35}S_2$ starts around 1.3 V and the current densities reach 1000 mA cm^{-2} at 2.0 V. Proof of concept electrolysers of this type typically report current densities of 10–100 mA cm^{-2} at similar potential values[24].

To explain the fundamental mechanisms responsible for the catalytic performance of 2H $Nb_{1.35}S_2$, we calculated the thermodynamics of the limiting reaction—the adsorption of hydrogen on the catalyst surface using density functional theory including van der Waals interactions. It is well known that the best HER catalysts possess $\Delta G \sim 0$ (that is, the thermoneutral condition where change in free energy, *G*, is close to zero) so that there is a driving force for hydrogen adsorption on the active site but the binding energy is low to allow efficient hydrogen evolution. The results of the calculations are shown in Fig. 4. Our theoretical results suggest that both the Nb and S terminations are stable for the $Nb_{1.35}S_2$ phases. We have observed the Nb-terminated surface by STEM imaging (see Supplementary Fig. 3d). It can be seen in Fig. 4a that the free energy for hydrogen adsorption for the 2H $Nb_{1.35}S_2$ is close to being thermoneutral (~0.11 eV) when the surface is terminated by Nb under 0.25 monolayer coverage (Fig. 4b). In contrast, the free energy of adsorbed hydrogen is ~1 eV when the surface is terminated by sulfur in 2H $Nb_{1.35}S_2$. The calculations also reveal that the reaction is localized to the surface of the catalysts, as indicated by the charge density diagrams in Fig. 4c. The HER properties of the 2H $Nb_{1.35}S_2$ relative to the 3R $Nb_{1.35}S_2$ are consistent with the higher density of states at the Fermi level (Fig. 4e,f), which translates into higher measured conductivity and better charge transfer kinetics. Thus, our work provides insight into materials design for achieving high current densities with non-precious metal catalysts.

Online content

Any methods, additional references, Nature Research reporting summaries, source data, statements of code and data availability and associated accession codes are available at https://doi.org/10.1038/s41563-019-0463-8.

Received: 18 April 2018; Accepted: 15 July 2019;
Published online: 26 August 2019

References

1. Lukowski, M. A. et al. Enhanced hydrogen evolution catalysis from chemically exfoliated metallic MoS_2 nanosheets. *J. Am. Chem. Soc.* **135**, 10274–10277 (2013).
2. Voiry, D. et al. Conducting MoS_2 nanosheets as catalysts for hydrogen evolution reaction. *Nano Lett.* **13**, 6222–6227 (2013).
3. Voiry, D. et al. Enhanced catalytic activity in strained chemically exfoliated WS_2 nanosheets for hydrogen evolution. *Nat. Mater.* **12**, 850 (2013).
4. Liu, Y. et al. Self-optimizing, highly surface-active layered metal dichalcogenide catalysts for hydrogen evolution. *Nat. Energy* **2**, 17127 (2017).
5. Shi, J. et al. Two-dimensional metallic tantalum disulfide as a hydrogen evolution catalyst. *Nat. Commun.* **8**, 958 (2017).
6. Li, H. et al. Atomic-sized pores enhanced electrocatalysis of TaS2 nanosheets for hydrogen evolution. *Adv. Mater.* **28**, 8945–8949 (2016).
7. Yuan, J. et al. Facile synthesis of single crystal vanadium disulfide nanosheets by chemical vapor deposition for efficient hydrogen evolution reaction. *Adv. Mater.* **27**, 5605–5609 (2015).
8. Chia, X., Ambrosi, A., Lazar, P., Sofer, Z. & Pumera, M. Electrocatalysis of layered Group 5 metallic transition metal dichalcogenides (*MX*2, *M* = V, Nb, and Ta; *X* = S, Se, and Te). *J. Mater. Chem. A* **4**, 14241–14253 (2016).
9. Jaramillo, T. F. et al. Identification of active edge sites for electrochemical H2 evolution from MoS_2 nanocatalysts. *Science* **317**, 100–102 (2007).
10. Zhigang, S., Baolian, Y. & Ming, H. Bifunctional electrodes with a thin catalyst layer for 'unitized' proton exchange membrane regenerative fuel cell. *J. Power Sources* **79**, 82–85 (1999).
11. Altmann, S., Kaz, T. & Friedrich, K. A. Bifunctional electrodes for unitised regenerative fuel cells. *Electrochim. Acta* **56**, 4287–4293 (2011).
12. Jellinek, F., Brauer, G. & Müller, H. Molybdenum and niobium sulphides. *Nature* **185**, 376 (1960).
13. Merki, D. & Hu, X. Recent developments of molybdenum and tungsten sulfides as hydrogen evolution catalysts. *Energy Environ. Sci.* **4**, 3878–3888 (2011).
14. Benck, J. D., Hellstern, T. R., Kibsgaard, J., Chakthranont, P. & Jaramillo, T. F. Catalyzing the hydrogen evolution reaction (HER) with molybdenum sulfide nanomaterials. *ACS Catal.* **4**, 3957–3971 (2014).
15. Voiry, D. et al. The role of electronic coupling between substrate and 2D MoS_2 nanosheets in electrocatalytic production of hydrogen. *Nat. Mater.* **15**, 1003 (2016).
16. Yin, Y. et al. Contributions of phase, sulfur vacancies, and edges to the hydrogen evolution reaction catalytic activity of porous molybdenum disulfide nanosheets. *J. Am. Chem. Soc.* **138**, 7965–7972 (2016).
17. Kibsgaard, J., Chen, Z., Reinecke, B. N. & Jaramillo, T. F. Engineering the surface structure of MoS_2 to preferentially expose active edge sites for electrocatalysis. *Nat. Mater.* **11**, 963 (2012).
18. Kong, D. et al. Synthesis of MoS_2 and $MoSe_2$ films with vertically aligned layers. *Nano Lett.* **13**, 1341–1347 (2013).
19. Tsai, C., Abild-Pedersen, F. & Nørskov, J. K. Tuning the MoS2 edge-site activity for hydrogen evolution via support interactions. *Nano Lett.* **14**, 1381–1387 (2014).

20. Eda, G. et al. Photoluminescence from chemically exfoliated MoS_2. *Nano Lett.* **11**, 5111–5116 (2011).
21. Pan, H. Metal dichalcogenides monolayers: novel catalysts for electrochemical hydrogen production. *Sci. Rep.* **4**, 5348 (2014).
22. Tsai, C., Chan, K., Nørskov, J. K. & Abild-Pedersen, F. Theoretical insights into the hydrogen evolution activity of layered transition metal dichalcogenides. *Surf. Sci.* **640**, 133–140 (2015).
23. Yu, Y. et al. Layer-dependent electrocatalysis of MoS_2 for hydrogen evolution. *Nano Lett.* **14**, 553–558 (2014).
24. Han, N. et al. Nitrogen-doped tungsten carbide nanoarray as an efficient bifunctional electrocatalyst for water splitting in acid. *Nat. Commun.* **9**, 924 (2018).
25. Kibsgaard, J., Jaramillo, T. F. & Besenbacher, F. Building an appropriate active-site motif into a hydrogen-evolution catalyst with thiomolybdate $[Mo_3S_{13}]^{2-}$ clusters. *Nat. Chem.* **6**, 248 (2014).
26. Xie, J. et al. Defect-rich MoS_2 ultrathin nanosheets with additional active edge sites for enhanced electrocatalytic hydrogen evolution. *Adv. Mater.* **25**, 5807–5813 (2013).
27. Hellstern, T. R., Benck, J. D., Kibsgaard, J., Hahn, C. & Jaramillo, T. F. Engineering cobalt phosphide (CoP) thin film catalysts for enhanced hydrogen evolution activity on silicon photocathodes. *Adv. Energy Mater.* **6**, 1501758 (2016).
28. Wu, T. et al. Crystallographic facet dependence of the hydrogen evolution reaction on CoPS: theory and experiments. *ACS Catal.* **8**, 1143–1152 (2018).
29. Li, H. et al. Activating and optimizing MoS_2 basal planes for hydrogen evolution through the formation of strained sulphur vacancies. *Nat. Mater.* **15**, 48 (2016).

Acknowledgements

M.C. and J.Y. acknowledge financial support from AFOSR grant no. FA9550-16-1-0289. M.C. and Y.W. acknowledge support from NSF grant no. ECCS-1608389. M.C., W.Z. and X.S. acknowledge support from Shenzhen Peacock Plan (grant no. KQTD2016053112042971). M.C. and A.R.M. acknowledge financial support from the Ministry of Higher Education Malaysia. H.Y.J. acknowledges support from Creative Materials Discovery Programme through the National Research Foundation of Korea (grant no. NRF-2016M3D1A1900035). E.J.G.S. acknowledges the use of computational resources from the UK National High-performance Computing Service (ARCHER) for which access was obtained via the UKCP consortium (EPSRC grant no. EP/K013564/1), and the UK Materials and Molecular Modelling Hub for access to the THOMAS supercluster, which is partially funded by EPSRC (grant no. EP/P020194/1). The Queen's Fellow Award through grant no. M8407MPH, the Enabling Fund (grant no. A5047TSL) and the Department for the Economy (grant no. USI 097) are also acknowledged by E.J.G.S.

Author contributions

M.C. conceived the idea and supervised the project. J.Y. and A.R.M. designed the experiments with guidance from M.C. J.Y. performed the electrochemical measurements and analyses with advice from R.F. and D.V. A.R.M. synthesized the $Nb_{1.35}S_2$ samples and characterized them. Y.W. made the devices for the HER measurements and took the electrical measurements. X.S. and I.B. made the NbS_2 samples and characterized them with the help of F.Z. and W.Z. H.Y.J. prepared the focused ion beam samples and performed the STEM analyses on the samples. M.A. and E.J.G.S. provided theoretical insight for the experimental results. M.C., H.Y.J., J.Y., D.V., R.F. and H.S.S. analysed the data. M.C. wrote the paper with J.Y. and all of the authors edited the manuscript before submission.

Competing interests

The authors declare no competing interests.

Additional information

Supplementary information is available for this paper at https://doi.org/10.1038/s41563-019-0463-8.

Reprints and permissions information is available at www.nature.com/reprints.

Correspondence and requests for materials should be addressed to E.J.G.S., H.Y.J. or M.C.

Publisher's note: Springer Nature remains neutral with regard to jurisdictional claims in published maps and institutional affiliations.

Methods

Growth of 2H $Nb_{1+x}S_2$ and 3R $Nb_{1+x}S_2$. $Nb_{1+x}S_2$ growth was achieved under low pressure in a horizontal furnace (Lindberg/Blue M) with a 25-mm diameter quartz tube. Two small quartz tubes (diameter ~ 9 mm) loaded with niobium chloride ($NbCl_5$, Alfa Aesar, 99.9%) and sulfur powder (Alfa Aesar, 99.5%) were placed upstream of the furnace as shown in Supplementary Fig. 6. The substrates (SiO_2/Si and glassy carbon) were placed face up above an alumina boat in the centre zone of the furnace. The tube was initially pumped to a base pressure of 20 Torr for 30 min. The furnace was heated up to 850 °C with a ramp rate of 55 °C min^{-1} with a flow of 90 sccm Ar. Then, the furnace was heated up to 1,000 °C with a ramp rate of 6 °C min^{-1} under a flow of 90 sccm (standard cubic centimetres) H_2/Ar (10% H_2 in Ar). The $NbCl_5$ was sublimated via a heating belt at 260–300 °C within 5 min when the furnace reached 1,000 °C as indicated by the heating cycle shown in Supplementary Fig. 7. After growth for 8 min at 1,000 °C, the whole system was naturally cooled down to room temperature.

Synthesis of 2H NbS_2. 2H NbS_2 was synthesized by CVD using niobium oxide (Nb_2O_5, 99.9% Sigma-Aldrich) mixed with alkali halide (potassium iodine, KI) and sulfur powder (99.5%, Alfa Aesar). Since niobium oxide has a high melting point, alkali halide is used to create a new eutectic point for the reaction to produce more volatile oxides[30]. The mixture of 150 mg of Nb_2O_5 and 100 mg of KI powders in the alumina boat was loaded at the centre of the tube furnace and SiO_2 substrates were placed above the powder with their polished side facing down. Then 100 mg of S powder was loaded into the upstream region of the tube. To remove oxygen in the furnace, 80 sccm carrier gas (10% of H_2 in Ar) was introduced for 20 min. The furnace was heated with a ramp rate of 33 °C min^{-1} to the growth temperatures (1,000 °C) and then held at 1,000 °C for 30 min before cooling down. The upstream region reached 200 °C during growth. The thin 2H NbS_2 crystals and their corresponding Raman spectrum are shown in Supplementary Fig. 8a,b.

Synthesis of 3R NbS_2. 3R NbS_2 crystals were grown by a chemical vapour transport method, which has been employed to prepare other layered compounds[31]. Before crystal growth, a quartz tube containing high-purity source (Nb 99.99% and S 99.99% with a molar ratio of Nb:S of 1:2) was evacuated at 10^{-6} Torr and sealed. The sealed quartz tube was then inserted into the tube furnace. The furnace was heated up to 900 °C with a ramp rate of 3 °C min^{-1}. The reaction time was 18 h at 900 °C and the furnace was cooled down naturally. The 3R crystals grown by chemical vapour transport and the corresponding Raman spectrum are shown in Supplementary Fig. 8c,d.

Electrochemical measurements. Electrochemical measurements were performed in a three-electrode cell using a Versa Stat 3 potentiostat from Princeton Applied Research. All measurements were made in 0.5 M H_2SO_4 electrolyte purged with Ar gas. A saturated calomel electrode (SCE, Pine Instruments) and glassy carbon were used as the reference electrode and counter electrode, respectively. Supplementary Fig. 9 shows the polarization curves obtained from 2H $Nb_{1.35}S_2$ using the platinum and carbon counter electrodes. No noticeable difference was observed, and this excludes any Pt contamination during the measurements. The glassy carbon plate (Ted Pella) loaded with 3R and 2H $Nb_{1.35}S_2$ was used as a working electrode. 3R NbS_2 was dispersed into toluene and sonicated for 1 h. The solution was deposited onto the glassy carbon electrode (0.1 mg cm^{-2}) and dried. 1T MoS_2 was prepared by the exfoliation of 2H MoS_2 by *n*-butyllithium following the literature[20]. 1T MoS_2 solution was loaded onto the glassy carbon electrode (4 μg cm^{-2}) and 2H MoS_2 powder dispersed into the mixed solution with DI (de-ionized) water/IPA (isopropyl alcohol at volume ratio 4:1). The MoS_2 in DI/IPA solution was sonicated for 1 h to dropped onto the glassy carbon electrode. All polarization curves were measured at the scan rate of 5 mV s^{-1}. All potentials are referenced to RHE. In 0.5 M H_2SO_4, E(potential)(RHE) = E(SCE) + 0.254 V. Impedance measurements were performed at −0.22 V versus a RHE from 1 MHz to 0.1 Hz with a 5 mV a.c. (alternating current) amplitude.

Device fabrication of 2H NbS_2. To demonstrate the HER performance of 2H NbS_2, we carried out the HER test using an electrochemical microcell[15]. We performed electron-beam lithography to put gold contacts on as-grown 2H NbS_2 on SiO_2 (300 nm) substrate. The gold electrodes were deposited via electron-beam evaporation under high-vacuum conditions (10^{-7} Torr). After this process, we performed another electron-beam lithography step to open a window on 2H NbS_2 and cover the gold electrodes to avoid contact with the electrolyte. The device is shown in Supplementary Fig. 10. Electrochemical measurements were performed in 0.5 M H_2SO_4, and glassy carbon and Ag/AgCl electrodes were used as counter and reference electrodes, respectively.

Electrochemical surface area measurements. The estimation of electrochemically active surface area was conducted by measurement of the double-layer capacitance in a potential region with no Faradaic response. Cyclic voltammetric measurements were performed between 285 mV and 315 mV versus a RHE at various scan rates from 5 mV s^{-1} to 100 mV s^{-1} to estimate the double-layer capacitance (C_{dl}), see Supplementary Fig. 5. Roughness factor (RF) was estimated from the ratio of the measured double-layer capacitance with respect to the specific capacitance of the glassy carbon electrode (0.87 mF cm^{-2}). Our image analysis of the electrode surface (Supplementary Fig. 5) shows that only ~20% of the glassy carbon electrode is covered by the catalyst. Therefore, to calculate the RF, we take the areal capacitance of the glassy carbon after catalyst deposition to be (0.87 mF cm^{-2}) × (0.8) = 0.7 mF cm^{-2}. Thus, the RF is given by:

$$\mathrm{RF} = \frac{9.6\ \mathrm{mF\ cm^{-2}}}{0.7\ \mathrm{mF\ cm^{-2}}} = 13.7$$

Turnover frequency calculation. According to previous literature, turnover frequency can be obtained from the following equation:

$$\mathrm{TOF}(s^{-1}) = \frac{J(\mathrm{A\ cm^{-2}})}{n \times N \times \mathrm{RF} \times (1.602 \times 10^{-19}\ \mathrm{C})}$$

To determine the density of active sites (N), we assume the lattice constant of 2H $Nb_{1.35}S_2$ to be 3.31 Å (Fig. 1c, STEM image); n is the number of electrons involved in the reaction. The surface area of the unit cell is 9.4×10^{-16} cm^2. We assumed that the entire basal plane can be catalytically active. Therefore, the density of active sites is estimated to be about 1.06×10^{15} cm^{-2}. The density of the surface active sites of 2H $Nb_{1.35}S_2$ on the geometric area is 1.06×10^{15} sites cm^{-2} $\times 13.7 = 1.4 \times 10^{16}$ sites cm^{-2}.

To get TOF at the exchange current density, the exchange current density was extrapolated linearly from the Tafel slope. The exchange current density of 2H $Nb_{1.35}S_2$ is 800 μA m^{-2} can be compared with other TMD based catalyst values listed in Supplementary Table 1.

Electrical conductivity measurements. The conductivity of the phases was measured by evaporating gold contacts and is shown in Supplementary Fig. 11. We find the 2H $Nb_{1.35}S_2$ phase to be highly conducting compared to other reports in the literature[32–35].

Computational methods. The calculations were carried out using plane-wave density functional theory and the Vienna ab initio simulation package[36–39]. The van der Waals interactions were taken into account at the level of opt-B88 functional[40] and the Bayesian error estimation exchange-correlation functional with long-range interactions[41] (BEEF-vdW). A 500 eV plane-wave cutoff was used, and the Brillouin zone was sampled with a Monkhorst–Pack[42] sampling of $3 \times 3 \times 1$ k-point grid for the relaxation and a $15 \times 15 \times 1$ k-point grid for the energy calculations. Then the free energy for the limiting reaction, ΔG_H, were calculated using the formula:

$$\Delta G_H = \Delta E + \Delta(\mathrm{ZPE}) - T\Delta S$$

with

$$\Delta E = E(\mathrm{surface} + \mathrm{H}) - E(\mathrm{surface}) - \tfrac{1}{2}E(\mathrm{H_2})$$
$$\Delta(\mathrm{ZPE}) = ZPE_H - \tfrac{1}{2}\mathrm{ZPE_{H_2}}$$
$$T\Delta S = -\tfrac{1}{2}TS_{\mathrm{H_2}} = -0.205\ \mathrm{eV}$$

where S is the entropy, E(surface + H) is the total energy of the system with the H-adatom bound at the basal plane, E(surface) is the total energy of the pristine system and $E(H_2)$ is the total energy of the H_2 molecule; Δ(ZPE) is the difference between the zero-point energy (ZPE) of the H-adatom and the ZPE of the H_2 molecule, calculated using the normal mode analysis. We will use the entropy of the molecular hydrogen in the gas phase at standard conditions (1 bar of H_2, pH = 0 and temperature T = 300 K).

The bulk lattice parameters calculated using ab initio opt B88-vdW and BEEF-vdW functionals are shown in Supplementary Tables 3 and 5, and their energetics are displayed in Extended Tables 4, 6, 7 and 8. The corresponding crystal structures obtained from these parameters are shown in Supplementary Fig. 12.

Data availability

The data that support the findings of this study are available from the corresponding authors upon reasonable request.

References

30. Li, S. et al. Halide-assisted atmospheric pressure growth of large WSe_2 and WS_2 monolayer crystals. *Appl. Mater. Today* **1**, 60–66 (2015).
31. Suh, J. et al. Doping against the native propensity of MoS_2: degenerate hole doping by cation substitution. *Nano Lett.* **14**, 6976–6982 (2014).
32. Huang, Y. H., Peng, C. C., Chen, R. S., Huang, Y. S. & Ho, C. H. Transport properties in semiconducting NbS_2 nanoflakes. *Appl. Phys. Lett.* **105**, 93106 (2014).

33. Molenda, J., Bak, T. & Marzec, J. Electrical and electrochemical properties of niobium disulphide. *Phys. Status Solidi A* **156**, 159–168 (1996).
34. Niazi, A. & Rastogi, A. K. Low-temperature resistance minimum in non-superconducting 3R-$Nb_{1+x}S_2$ and 3R-Ga_xNbS_2. *J. Phys. Condens. Matter* **13**, 6787 (2001).
35. Zhao, S. et al. Two-dimensional metallic NbS: growth, optical identification and transport properties. *2D Mater.* **3**, 25027 (2016).
36. Kresse, G. & Hafner, J. Ab initio molecular dynamics for liquid metals. *Phys. Rev. B* **47**, 558–561 (1993).
37. Kresse, G. & Hafner, J. Ab initio molecular-dynamics simulation of the liquid-metal–amorphous-semiconductor transition in germanium. *Phys. Rev. B* **49**, 14251–14269 (1994).
38. Kresse, G. & Furthmüller, J. Efficiency of ab-initio total energy calculations for metals and semiconductors using a plane-wave basis set. *Comput. Mater. Sci.* **6**, 15–50 (1996).
39. Kresse, G. & Furthmüller, J. Efficient iterative schemes for ab initio total-energy calculations using a plane-wave basis set. *Phys. Rev. B* **54**, 11169–11186 (1996).
40. Klimeš, J., Bowler, D. R. & Michaelides, A. Chemical accuracy for the van der Waals density functional. *J. Phys. Condens. Matter* **22**, 22201 (2010).
41. Wellendorff, J. et al. Density functionals for surface science: exchange-correlation model development with Bayesian error estimation. *Phys. Rev. B* **85**, 235149 (2012).
42. Monkhorst, H. J. & Pack, J. D. Special points for Brillouin-zone integrations. *Phys. Rev. B* **13**, 5188–5192 (1976).